Magnetic Resonance in Medicine 51:480–486 (2004)

Targeted Nanoparticles for Quantitative Imaging of Sparse Molecular Epitopes With MRI

Anne M. Morawski,[1] Patrick M. Winter,[1] Kathryn C. Crowder,[1] Shelton D. Caruthers,[1,2] Ralph W. Fuhrhop,[1] Michael J. Scott,[1] J. David Robertson,[3] Dana R. Abendschein,[1] Gregory M. Lanza,[1] and Samuel A. Wickline[1*]

Before molecular imaging with MRI can be applied clinically, certain problems, such as the potential sparseness of molecular epitopes on targeted cell surfaces, and the relative weakness of conventional targeted MR contrast agents, must be overcome. Accordingly, the conditions for diagnostic conspicuity that apply to any paramagnetic MRI contrast agent with known intrinsic relaxivity were examined in this study. A highly potent paramagnetic liquid perfluorocarbon nanoparticle contrast agent (~250 nm diameter, >90000 Gd^{3+}/particle) was imaged at 1.5 T and used to successfully predict a range of sparse concentrations in experimental phantoms with the use of standard MR signal models. Additionally, we cultured and targeted the smooth muscle cell (SMC) monolayers that express "tissue factor," a glycoprotein of crucial significance to hemostasis and response to vascular injury, by conjugating an anti-tissue factor antibody fragment to the nanoparticles to effect specific binding. Quantification of the signal from cell monolayers imaged at 1.5 T demonstrated, as predicted via modeling, that only *picomolar* concentrations of paramagnetic perfluorocarbon nanoparticles were required for the detection and quantification of tissue factor at clinical field strengths. Thus, for targeted paramagnetic agents carrying high payloads of gadolinium, it is possible to quantify molecular epitopes present in picomolar concentrations in single cells with routine MRI. Magn Reson Med 51:480–486, 2004. © 2004 Wiley-Liss, Inc.

Key words: magnetic resonance imaging; molecular imaging; contrast agents; nanoparticles; tissue factor

A principal aim of molecular imaging is to provide an in vivo analogue to immunohistochemistry that offers equivalent diagnostic accuracy and flexibility for delineating the expression of numerous proteins, and at the same time enables the noninvasive, nondestructive, and serial characterization of disease evolution. For these purposes, specific molecular contrast agents are under development that target selected molecular epitopes, which can be registered spatially by diverse imaging methods (1,2). Of the available candidate technologies for clinical in vivo molecular imaging, magnetic resonance (MR) methods offer unparalleled image resolution without the use of ionizing radiation.

The targeted contrast agents proposed for MR molecular imaging exhibit either superparamagnetic or paramagnetic properties that are typically used to generate negative or positive contrast enhancement, respectively (3). A potential hurdle for molecular imaging with paramagnetic MR contrast agents entails the anticipated sparseness of the molecular epitopes on targeted cell surfaces (e.g., nanomolar concentrations), in concert with the modest signal intensity from conventional paramagnetic contrast agents, which may result in insufficient contrast-to-noise ratio (CNR) for diagnostic imaging. Yet, to our knowledge, the limits of detectability for MRI of molecules that appear in sparse concentrations in early pathological processes have not been quantified for any targeted contrast agent. This step is critical for identifying those pathologies that might be amenable to diagnosis with MRI based on the expected concentration of available molecular targets.

Accordingly, we sought to elucidate the conditions for diagnostic conspicuity that apply to any paramagnetic agent with known intrinsic relaxivity. We corroborated our predictions by imaging a cellular epitope of crucial significance to vascular repair following injury: smooth muscle cell (SMC) tissue factor. Tissue factor is a transmembrane glycoprotein that is involved in a number of important physiological and pathological processes, including thrombosis, hemostasis, angiogenesis, cell signaling, and mitogenesis (4). For the molecular imaging contrast agent itself, we employed a highly potent paramagnetic perfluorocarbon nanoparticle to target SMC tissue factor by coupling a polyclonal anti-tissue factor antibody ligand (5–7). We recently showed that this system is capable of detecting angiogenesis in early atherosclerosis and experimental tumor models with great specificity (8,9). We both predicted and observed that only *picomolar* concentrations of paramagnetic perfluorocarbon nanoparticles are required for the detection and quantification of tissue factor on single SMC monolayers at clinical field strengths (1.5 T).

MATERIALS AND METHODS

Nanoparticle Emulsions

Methods developed in our laboratories were used to prepare perfluorocarbon emulsions encapsulated by a lipid-surfactant monolayer (10,11). The perfluorocarbon emulsions consisted of perfluorooctylbromide (PFOB, 40% vol/vol), a surfactant comixture (2% wt/vol), and glycerol

[1]Cardiovascular MR Laboratories, Washington University School of Medicine, St. Louis, Missouri.

[2]Philips Medical Systems, Best, The Netherlands.

[3]Research Reactor Center (MURR), University of Missouri–Columbia, Columbia, Missouri.

Grant sponsor: National Institutes of Health; Grant numbers: HL-42950; HL-59865; NO1-C0-07121; Grant sponsors: American Heart Association; Barnes-Jewish Research Foundation; Edith and Alan Wolff Charitable Trust; Philips Medical Systems.

*Correspondence to: Samuel A. Wickline, M.D., Washington University School of Medicine, Campus Box 8086, 660 South Euclid Ave., St. Louis, MO 63110. E-mail: saw@howdy.wustl.edu

Received 22 July 2003; revised 21 October 2003; accepted 29 October 2003.

DOI 10.1002/mrm.20010

Published online in Wiley InterScience (www.interscience.wiley.com).

(1.7% wt/vol), with deionized water comprising the balance. Approximately 92400 paramagnetic chelates (Gd-DTPA-BOA) were formulated onto the surface of each particle, as previously described (12). The nominal size for each formulation was measured with a Malvern Zetasizer submicron particle analyzer (Malvern Instruments, Worchestershire, UK). Neutron activation analysis was carried out as described below to determine the exact concentration of gadolinium on the particles for assessment of particle relaxivity.

Relaxivity measurements were obtained for the emulsion at both 1.5 T and 4.7 T (12). Briefly, spin-echo (SE) and inversion recovery (IR) images of six nanoparticle dilutions were obtained from a 1.5T clinical scanner (NT Intera CV; Philips Medical Systems, Best, Netherlands) with a standard 11-cm-diameter surface coil. T_1 measurements were calculated from the real component of the images collected with an IR MRI pulse sequence, while T_2 was calculated from SE images with various echo times (TE). Relaxivity measurements were similarly determined with a 4.7 T magnet interfaced to a Varian INOVA console (Varian Associates, Palo Alto, CA) and a 5-cm-diameter birdcage coil.

Nanoparticle Phantoms

Six nanoparticle test phantoms were prepared in centrifuge tubes. A base solution of glycerine (40% vol/vol) and deionized water was formulated to have relaxation times similar to those of blood ($T_1 \approx 1200$ ms, $T_2 \approx 50$ ms). Selected volumes of the nanoparticle emulsion were added to five of the six phantoms.

After imaging, the gadolinium content of each phantom was analyzed by standard neutron activation techniques conducted at the University of Missouri Research Reactor facility (MURR). Briefly, the samples were placed in specialized plastic cuvettes that contained no interfering metals. They were weighed wet, lyophilized, and reweighed. We determined the mass of gadolinium by measuring the 361 keV gamma rays from the beta decay of ^{161}Gd ($T_{1/2}$ = 3.66 min) produced through neutron capture on ^{160}Gd. Individual samples and standards were irradiated in a thermal neutron flux of about 5×10^{13} n · cm^{-2} · s^{-1} for 7 s, allowed to decay for 30 s, and counted on a high-resolution gamma-ray spectrometer for 300 s. For this method, the minimum detectable amount of gadolinium is reported to be several nanograms (13).

SMC Cultures

We prepared 18 cultures of porcine aortic SMCs by plating 50000 cells on each 1.0-cm culture plate insert (Millipore, Bedford, MA) and allowing them to grow for 2 days to approximately 200000 cells per insert. We derived the primary cultures used as sources for these experiments by digesting adult pig aortic segments in trypsin, and then passaging cultures four times to enrich the SMC population. We have shown previously that these cultured cells constitutively express tissue factor (7).

To target tissue factor on the cell surface, we generated a polyclonal antibody to the extracellular domain of recombinant porcine tissue factor (derived from *Eschericia coli*; residues 1–208 (MW 22.8 kD)) in rabbits (provided by E. Tolunay, Monsanto Co., St. Louis, MO) according to previously described methods (5,14,15). These antibodies were purified, washed with 20 mmol/L sodium phosphate, eluted with 0.1 mol/L glycine-HCl, and neutralized with 1 mol/L Tris buffer. The anti-tissue factor antibody was then biotinylated according to standard methods for use as a targeting ligand.

Nanoparticles were targeted to tissue factor receptors on cultured cells ($N = 6$) by the use of a convenient three-step pretargeting strategy: 1) exposure to excess biotinylated anti-tissue factor antibody, 2) treatment with avidin (Pierce Chemical Co.), and 3) exposure to biotinylated perfluorocarbon nanoparticle emulsion. The cell cultures were washed between each step. The nontargeted cell cultures ($N = 6$) were treated in the same manner, but without initial administration of the biotinylated antibody. The control cell cultures ($N = 6$) were left untreated. The culture plate inserts were then filled with a 1.5% agarose gel solution to preserve the cells for MRI at 1.5T.

MRI

All images were acquired on a 1.5T clinical scanner with a quadrature birdcage receiver coil. All T_1, T_2, and proton density measurements were obtained with a mixed SE and IR sequence (TE = 30 ms, eight echoes, two averages per scan, slice thickness = 3 mm, SE TR = 1000 ms, IR TR = 1500 ms, inversion time (TI) = 500 ms, and in-plane resolution for phantoms = 0.55 mm × 0.55 mm; and TE = 17 ms, one echo, 30 averages per scan, slice thickness = 2 mm, SE TR = 760 ms, IR TR = 2290 ms, TI = 370 ms, and in-plane resolution for the cell layers = 0.29 mm × 0.29 mm). The mixed-scanning protocol combines multiecho SE and IR acquisitions, and thus generates several images with different levels of T_1 and T_2 weightings (16). From these multiweighted images, T_1 and T_2 relaxation times and proton density can be calculated using RLSQ algorithms, which combine pixel value ratio and linear squared fitting operations. 2D SE images of both the phantoms and cells were acquired over a range of repetition times (TRs) (TE = 8 ms, two averages per scan, slice thickness = 3 mm, and in-plane resolution for phantoms = 0.55 mm × 0.55 mm; and TE = 15 ms, 20 averages per scan, slice thickness = 2 mm, and in-plane resolution for the cell layers = 0.29 mm by 0.29 mm). CNRs for the phantoms and cells in the SE images were calculated with reference to the nanoparticle phantom with no added particles and the control cell group, respectively. A 3D stack of T_1-weighted fast SE images (echo train length = 18, in-plane field of view (FOV) = 140 mm × 119 mm, in-plane resolution acquired at 0.28 mm × 0.28 mm reconstructed to 0.14 mm × 0.14 mm, through-plane FOV = 22.5 mm, slice thickness = 0.5 mm, TR = 364 ms, TE = 16 ms, 32 averages per scan) was used to generate the maximum intensity projection (MIP) through the plane of cell monolayers.

Gas Chromatography (GC)

The perfluorocarbon content in three of the six cell culture replicates was measured after treatment to determine the

Table 1
Relaxivity Data for the Perfluorocarbon Nanoparticle Emulsion at 1.5 T and 4.7 T

	Field Strength	
	1.5T	4.7T
Gd^{3+} ions per particle	94,200	
r_1 Relaxivity $(s*mM)^{-1}$ [Gd]	17.9 ± 0.6	9.7 ± 0.2
r_2 Relaxivity $(s*mM)^{-1}$ [Gd]	25.3 ± 0.6	29.4 ± 0.3
r_1 Relaxivity $(s*mM)^{-1}$ [Particle]	$1.69 \times 10^6 \pm 6 \times 10^4$	$0.91 \times 10^6 \pm 2 \times 10^4$
r_2 Relaxivity $(s*mM)^{-1}$ [Particle]	$2.38 \times 10^6 \pm 6 \times 10^4$	$2.8 \times 10^6 \pm 3 \times 10^4$

extent of nanoparticle binding with GC using flame ionization detection and a bonded phase column (model 6890; Agilent Technologies, Inc. Wilmington, DE). Each membrane was combined with 20% potassium hydroxide in methanol and homogenized into a uniform mixture. The suspension was then combined with 2.0 mL of internal standard (0.1% octane in freon), vigorously vortexed, and agitated continuously with a shaker for 30 min. The lower extracted layer was filtered through a silica gel column. The initial column temperature was 45°C, and this was ramped up to 145°C at a rate of 10°C/min.

We compared the quantitative MR data with the GC results by converting total perfluorocarbon content for each cell layer into concentration of nanoparticles in the scanned region. Briefly, surface area measurements for each cell layer were obtained from the MIP image. The total perfluorocarbon content was converted to number of nanoparticles using previously obtained GC data on the perfluorocarbon content of known volumes of emulsion. We approximated the volume of the cell monolayer by multiplying the total surface area from the MIP by the voxel height in the T_1 map. Dividing the total number of nanoparticles from GC by this volume resulted in an estimated nanoparticle concentration in each cell monolayer.

Signal Modeling

We assume that two adjacent tissues (A and B) manifest identical longitudinal (T_1) and transverse (T_2) relaxation times prior to nanoparticle binding, but only one tissue (B) expresses the molecular epitope of interest that binds the targeted paramagnetic nanoparticles. The bound paramagnetic nanoparticles affect the relaxation times in the targeted tissue according to the following equations (17):

$$\frac{1}{T_{1B}} = \frac{1}{T_{1A}} + r_{1P}[NP] \quad [1]$$

$$\frac{1}{T_{2B}} = \frac{1}{T_{2A}} + r_{2p}[NP], \quad [2]$$

where T_{1B} and T_{2B} are the observed relaxation times after the nanoparticle binding, T_{1A} and T_{2A} are the original relaxation times, r_{1p} and r_{2p} are the particle-based relaxivities, and [NP] represents the average nanoparticle concentration within the imaging voxel. For this simulation, we assume that targeted binding does not affect particle relaxivity (i.e., r_{1p} and r_{2p} remain constant).

The CNR between the two tissues for a given sequence is calculated as the absolute difference between their signal intensities. If I_A and I_B represent the signal intensities of tissues A and B, respectively, and N is the expected level of noise in the resulting image, the CNR is given as:

$$CNR = \left|\frac{I_A - I_B}{N}\right|. \quad [3]$$

For an SE pulse sequence, the signal intensity of each tissue is related to the chosen scan parameters (TE and TR) as well as its magnetic properties (T_1 and T_2), which change due to binding of the contrast agent, and is described with the following relationships for tissues A and B (18):

$$I_A = k_A(1 - 2e^{-(TR-TE/2)/T_{1A}} + e^{-TR/T_{1A}})e^{-TE/T_{2A}} \quad [4]$$

$$I_B = k_B(1 - 2e^{-(TR-TE/2)/T_{1B}} + e^{-TR/T_{1B}})e^{-TE/T_{2B}}. \quad [5]$$

The constants k_A and k_B incorporate factors such as proton density, flip angle, and coil sensitivity. Since these tissues are assumed to be identical except for the binding of the contrast agent, k_A and k_B are identical except for relative coil sensitivity to the positional differences between the two tissues for this simulation. Substituting Eqs. [4] and [5] into Eq. [3] and optimizing the resulting equation for TR provides a relationship between the T_1 values for the two tissues and the TR that will create the highest CNR (18):

$$TR_{opt} = \frac{T_{1A}T_{1B}}{T_{1B}-T_{1A}}\ln\left(\frac{k_A T_{1B}}{k_B T_{1A}}\right). \quad [6]$$

With the use of the field-dependent input parameters specified in Table 1, model predictions for the minimum concentration of contrast agent required to generate visually apparent contrast between the two tissues were determined. Visually apparent contrast was defined as a CNR $\geq$ 5 (19).

Statistical Analysis

We evaluated differences between the treatment groups for significance by analysis of variance (ANOVA), using the Statistical Analysis System (SAS, Cary, NC). A *P*-value of 0.05 was considered statistically significant.

RESULTS

Nanoparticle Characteristics

The nanoparticles were approximately 273 nm in diameter (polydispersity 0.15), corresponding to a nanoparticle con-

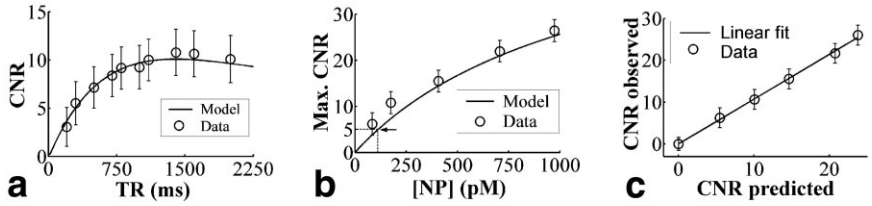

FIG. 1. **a:** CNR response (mean ± SD) in phantoms for a specific concentration of nanoparticles (176 pM) as predicted by the model and observed in a nanoparticle phantom imaged with an SE sequence (at 1.5T) over a range of TRs. **b:** Maximum CNR obtainable with selected concentrations of nanoparticles ([NP]), as predicted by the model and observed in the phantom experiments. The model predicts that the "minimum required" nanoparticle concentration (or the amount that yields a CNR of 5) is 113 picomolar. **c:** CNR measured in the phantoms (mean ± SD) at the optimum TR plotted against the CNR predicted by the model for the same concentration of nanoparticles. The linear regression line has a slope of 1.07 and an intercept of 0.049 ($r = 0.999$; P-value < 0.0001).

centration of 59 nM in the final emulsion. Neutron activation analysis indicated 6.17 mmol gadolinium (Gd^{3+}) per liter of emulsion or about 94200 Gd^{3+} atoms/particle. Table 1 shows the "ionic-based" r_1 and r_2 values for paramagnetic nanoparticles expressed per mM Gd^{3+}: 17.9 ± 0.6 and 25.3 ± 0.6 $(s \cdot mM)^{-1}$, respectively. For 1.5 T field strengths, the "particle-based" relaxivities that reflect the signal effects achievable per individual binding site (i.e., one particle) were 1690000 ± 100000, and 2380000 ± 60000 $(s \cdot mM\ particle)^{-1}$ for r_1 and r_2, respectively. At higher field strengths (4.7 T), this potency is preserved, although the r_1 declines whereas the r_2 increases slightly.

Nanoparticle Phantom Imaging

The T_1 measurements from concurrent imaging of the phantoms at 1.5T and gadolinium content of the samples measured by neutron activation analysis corresponded to final particle concentrations of 84 ± 2.8, 176 ± 5.9, 407 ± 14, 707 ± 24, and 974 ± 33 pM in the separate samples. Using these concentrations as inputs to the signal modeling algorithm, we were able to compare the predicted contrast response with actual contrast data obtained by imaging the phantoms with a traditional SE sequence. As shown in Eq. [6], for instance, the relationship between CNR and the TR used in the SE sequence indicates that the maximum effect of a given concentration of nanoparticles on contrast is realized at some determinable optimal TR (TR_{opt}). The model accurately identified this peak for all five phantoms, and predicted the substantial loss in contrast that occurs with increasing or decreasing TR (Fig. 1a). For example, imaging 300–400 ms below the optimum TR produced a loss in contrast of up to 25% according to both the phantom data and the model. Given this reduction in contrast at TRs that were much greater or less than the optimum, we based the subsequent model predictions on MR images acquired with the optimum TR.

An examination of the relationship between nanoparticle concentration and maximum CNR indicates that increases in diagnostic conspicuity should occur in concert with increasing concentrations of targeted nanoparticles. This notion is supported by the experimental data concerning the paramagnetic contrast agent performance obtained from phantom imaging as well as the quantitative model predictions (Fig. 1b). The inverse relationship between T_1 and nanoparticle concentration (see Eq. [4]) accounts for the nonlinear increase in contrast, resulting in a modest leveling of the contrast effect at high concentrations when TE is kept to a minimum (~7 nM). The close agreement between the model and the phantom data supports extrapolations to lower concentrations of nanoparticles (Fig. 1c). If a CNR ≥ 5 is defined as the minimum diagnostically meaningful contrast, the model shows that only picomolar concentrations of nanoparticles need be present within a typically-sized imaging voxel to produce diagnostic contrast enhancement for molecular imaging.

SMC Tissue Factor Imaging

Figure 2a indicates that the increase in longitudinal relaxation rate (R_1) after application of the nanoparticles was statistically significant for the targeted cells as compared to both the nontargeted and untreated cell layers. The concentration of nanoparticles calculated from the measured T_1 changes observed in the targeted cells (468 ± 30.3 pM) substantially exceeded the predicted threshold required to produce a CNR > 5 (113 pM). A low but significant level of nonspecific binding of the particles was observed in the cell cultures, most likely due to an incomplete washing procedure. However, the concentration of nanoparticles on the nontargeted-cell cultures (88 ± 3.3 pM) fell below the threshold for diagnostic conspicuity. The calculated CNR for targeted and nontargeted cells as compared to untreated cells was 17.7 and 4.7, respectively.

We confirmed the predicted nanoparticle concentrations by measuring the total perfluorocarbon content of the SMC samples with GC. The absolute concentration of nanoparticles bound to the targeted cell monolayers substantially exceeded that for the nontargeted layers (530 ± 42.8 vs. 111 ± 25.9 pM, respectively; $P < 0.0011$). These values did not differ significantly from those predicted from T_1 measurements (see above). The relationship between cellular nanoparticle concentrations determined by GC and MRI from T_1 measurements was linear, with a slope of 1.09 and intercept of 16 pM ($r = 0.97$; $P < 0.0016$).

The contrast response of the cell layers visibly varied with TR for otherwise identical SE scanning sequences. This quantitative dependence of contrast on TR was predicted accurately by the model for both the targeted and nontargeted cell layers (Fig. 2b). The greatest contrast between the targeted and untreated cell monolayers was observed for a TR of 900 ms (Fig. 2c). With the use of a standard 3D imaging technique, we generated substantial contrast between the targeted cell monolayers and the

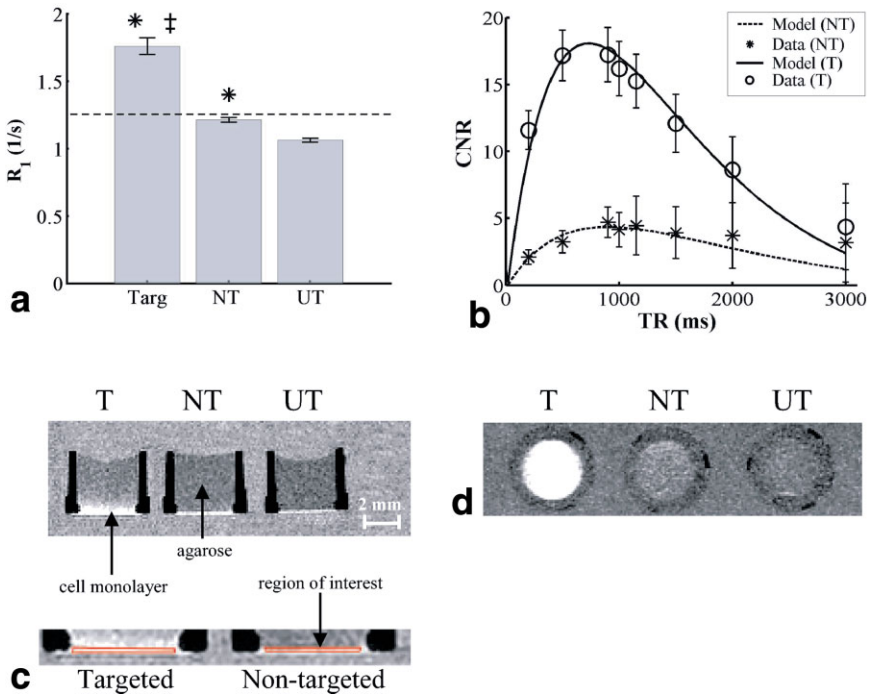

FIG. 2. **a:** Measured relaxation rates (mean ± SEM) in cellular monolayers for the three treatment groups (six replicates each), with * designating a statistical difference (P-value < 0.05) from untreated cells, and (‡) designating a statistical difference from nontargeted cells. Targeted (T) cells are shown on the left, nontargeted (NT) in the center, and untreated (UT) cells on the right. The dotted line indicates the lowest relaxation rate that will produce a CNR ≥ 5. **b:** CNR for targeted and nontargeted cell layers over a range of TRs, as observed in the SE experiment (mean ± SD) and predicted by the model. **c:** SE images of SMC monolayers (one replicate of each is shown) acquired with the optimum TR of 900 ms. The magnified inset of the targeted and nontargeted layers shows the region of interest (ROI; outlined in red) used to obtain the signal intensity measurements. ROIs were selected from T_1 maps of the cell monolayers and applied to all subsequent images. **d:** An MIP through a 3D stack of T_1-weighted images acquired parallel to the cell monolayers shown for one representative replicate demonstrates the sensitivity of this targeting method for displaying individual cells at clinical field strengths.

other treatment groups, and demonstrated the increased sensitivity of this agent for displaying individual cells at 1.5 T (Fig. 2d).

Modeling Greater Field Strengths and Alternative Nanoparticle Formulations

As a corollary to the primary model predictions, we also examined the theoretical influence of field strength, contrast agent relaxivity, and nanoparticle concentration on signal strength. Using the input parameters specified in Fig. 3a, we computed the minimum nanoparticle concentration required to produce a CNR of 5 at 1.5T and 4.7T over a range of hypothetical particle relaxivities. Figure 3b shows that greater field strengths should enhance the signal such that lower nanoparticle concentrations will be required for diagnosis, because the curve for the 4.7T data falls below that of the 1.5T data at all relaxivities. However, the incremental effectiveness of augmented particle relaxivity is not linear and tapers off at higher values of r_1, indicating diminishing returns for improvements in the performance of paramagnetic contrast agents when expressed per mM Gd, as previously suggested (20). This relationship has important implications for contrast-agent design, in that efforts to increase ionic relaxivity of the particles will provide limited increases in CNR.

DISCUSSION AND CONCLUSIONS

Initially, "hot spot" imaging with paramagnetic agents was performed with gadolinium-conjugated antibodies; however, the concentration of metal ion was not sufficient to achieve diagnostic contrast enhancement based on alterations in longitudinal proton relaxation (21,22). Indeed, the general assumption is that millimolar concentrations of gadolinium are required at the site to produce adequate signal (23). More recent studies have recognized the need to deliver larger payloads of paramagnetic agents by conjugating gadolinium chelates to carriers such as particles, dendrimers, or other polymeric constructs (2). The present data illustrate several new concepts regarding molecular imaging with targeted paramagnetic nanoparticles: 1) picomolar binding is sufficient to achieve diagnostic contrast to noise levels if high payload particles are employed; 2) sparse molecular epitopes, such as tissue factor, can be imaged on cells at clinical field strengths under certain reasonable conditions; and 3) model-based predictions of the local concentrations of targeted paramagnetic agents are accurate if the fundamental characteristics of the agent are known.

Our perfluorocarbon-based nanoparticle contrast agent was designed specifically to exhibit ion-based r_1 relaxivities that substantially exceed those found in traditional blood pool contrast agents (see Table 1). We recently re-

a

Input Parameters	Field Strength (T) 1.5	4.7
Initial T1 (ms)	1120	1700
Initial T2 (ms)	100	100
TE (ms)	10	10
Noise (%)	1.5	0.48
Voxel volume (μL)	0.3	0.3

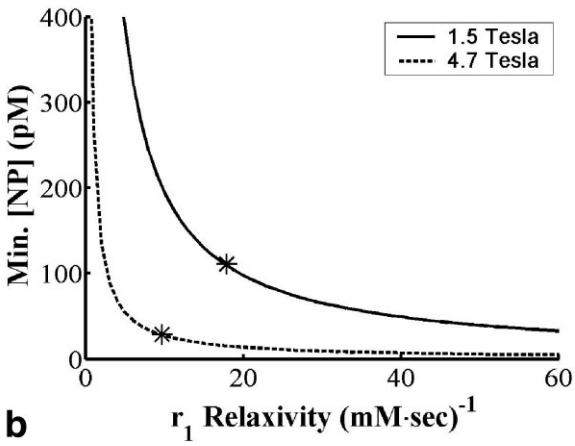

b

FIG. 3. **a:** Input parameters used in the model to compare imaging at 4.7 T with imaging at 1.5T. Relaxivity data for the nanoparticles for these field strengths are given in Table 1. **b:** Effect of altering the ionic r_1 relaxivity of the nanoparticles on the minimum concentration needed for diagnostic contrast at 1.5 T and 4.7 T. Transverse relaxivity (r_2) was assumed to be 1.5 times r_1 at 1.5 T, and 3 times r_1 at 4.7 T based on data obtained with the current formulation. The asterisks (*) indicate the ionic-based r_1 relaxivities of the current nanoparticle formulation at both field strengths (from Table 1).

ported that certain chemical modifications of the nanoparticle linker and chelating moieties can enhance ionic relaxivities up to 10-fold compared to current blood pool agents (12). Interestingly, the calculations shown in Fig. 3b suggest that attempts to influence T_1 relaxation might encounter diminishing returns if they focus *solely* on modifying the particle's ionic relaxivity (r_1). This behavior is a consequence of the fundamental multiexponential relationship between signal strength and the combined effects of local tissue paramagnetic properties, contrast agent concentration, and specific pulse sequence parameters, and the effects of the contrast agent itself (r_1 and r_2). Thus, adopting strategies that deliver more gadolinium to cells may be a more efficacious means of increasing lesion conspicuity with paramagnetic agents, which is better achieved with the use of higher payload agents, such as nanoparticles (16).

The present nanoparticle platform delivers a very large number of metal ions (~94200 Gd^{+3}/particle) to each binding site, which is the dominant mechanism responsible for the dramatic acceleration of local T_1 relaxation. This high paramagnetic payload enables surface molecular epitopes on cellular monolayers to be detected by the use of paramagnetic contrast agents that were formerly considered to be effective only in combination with superparamagnetic agents (see Fig. 2d) (24). For this agent, the particle-based relaxivity is amplified by a factor of $>10^6$ for the purposes of T_1-weighted targeted molecular imaging, and approximately 10^5 of that is due to the large local gadolinium concentration itself. For such a high level of relaxation enhancement to be produced, the particles must have a surface area large enough to encompass a high payload of metal ions. While larger particle sizes preclude extravasation into surrounding tissues and targeting of nonvascular cells, the multiplicity of physiologically important eptiopes on cells within the vasculature (e.g., fibrin, $\alpha_v\beta_3$, and tissue factor) provides a basis for targeted imaging of various disease processes, including atherosclerosis, post-angioplasty restenosis, and angiogenesis.

The CNR, which establishes a threshold for diagnostic conspicuity, is influenced by several factors, including the specific local concentration of paramagnetic nanoparticles that are bound to the selected molecular epitopes, the specific activity (relaxivity) of the agent itself, and the technical details of the imaging procedure. For example, low image resolution can attenuate the relaxation effects through partial volume dilution. The simulations inherently assume that the agent is uniformly distributed within a voxel. This may not be true in vivo, where the targeted cells may be a small fraction of the whole voxel. However, the relationship between the CNR and the nanoparticle concentration is approximately linear for the range of concentrations that would produce a CNR of ~20 (Fig. 1b). Therefore, as long as the weighted average concentration within the voxel is above the minimum detectable level, that group of cells will be clinically observable.

Awareness of the approximate lower limits of detection for a proposed molecular imaging platform is crucial for evaluating its potential performance in vivo. Several methods for optimizing contrast from nonspecific paramagnetic agents have been presented (20,25,26), and the basic principles of scan sequence optimization for optimal tissue contrast are well documented (27–29). However, the application of these principles to the emerging field of molecular imaging can provide invaluable insights into the development of paramagnetic agents for the diagnosis and treatment of disease. Such approaches allow the calculation of nanoparticle concentrations and CNR values for comparison with actual measurements of CNR in cell or tissue samples (see Fig. 2b). Absolute measurements of T_1 values to support such calculations can be readily obtained in vivo with conventional Look-Locker methods (30).

An additional unique aspect of this system is that one can confirm the local concentration of contrast agent independently by measuring the tissue perfluorocarbon content with GC. This could establish clinical MRI as a useful tool for contrast agent quantification for the first time. The relationships between nanoparticle concentrations calculated from actual T_1 values and measured by neutron activation or fluorine GC are linearly correlated (see Results). Furthermore, we have recently demonstrated that localized fluorine spectroscopy conducted on cellular

monolayers after particle binding yields a linear relationship between nanoparticle concentration and the fluorine signal (7). Thus, fluorine spectroscopy could confirm that the paramagnetic agent is responsible for the contrast enhancement observed in T_1-weighted images, as well as provide an alternative method of quantification, since there is little competing signal from fluorine in vivo.

By applying traditional signal modeling approaches, we were able to quantify the influence of paramagnetic nanoparticles on local relaxivities and compute the resulting contrast effect on T_1-weighted SE images. Both the model and experimental data indicate that picomolar quantities are effective for producing a diagnostic level of contrast with a 1.5T clinical scanner. From the concordance between the observed and predicted measures of CNR, and between the concentration of nanoparticles predicted from T_1 and measured by GC, we infer that the effective molecular relaxivities of the nanoparticle contrast agent after binding are similar to those measured in vitro—at least for the concentrations of molecular epitopes considered in this study.

Because the particle relaxivities appear to remain constant after binding, we propose that the contrast effect of this paramagnetic agent will remain predictable in clinical imaging situations involving sparse epitope concentrations. If this expectation is confirmed in future experiments, a method for quantitative MRI could result, which would enhance the utility of this agent and render it competitive with nuclear and PET imaging methods for the longitudinal assessment of epitope concentration and binding kinetics. We anticipate that this ability to predictably quantify local particle concentration will facilitate targeted drug/gene delivery with particulate carriers based on rational drug dosing that allows local rather than systemic concentrations of agents to be defined noninvasively (7,31,32).

REFERENCES

1. Weissleder R. Molecular imaging: exploring the next frontier. Radiology 1999;212:609–614.
2. Wickline SA, Lanza GM. Molecular imaging, targeted therapeutics, and nanoscience. J Cell Biochem 2002;39:90–97.
3. Gupta H, Weissleder R. Targeted contrast agents. Magn Reson Imaging Clin N Am 1996;4:171–184.
4. Kato H. Regulation of functions of vascular wall cells by tissue factor pathway inhibitor: basic and clinical aspects. Arterioscler Thromb Vasc Biol 2002;22:539–548.
5. Lanza GM, Abendschein DR, Hall CH, Marsh JN, Scott MJ, Scherrer DE, Wickline SA. Molecular imaging of stretch-induced tissue factor expression in carotid arteries with intravascular ultrasound. Invest Radiol 2000;35:227–234.
6. Lanza GM, Abendschein DR, Hall CH, Scott MJ, Scherrer DE, Houseman A, Miller JG, Wickline SA. In vivo molecular imaging of stretch-induced tissue factor in carotid arteries with ligand-targeted nanoparticles. J Am Soc Echocardiogr 2000;13:608–614.
7. Lanza GM, Yu X, Winter PM, Abendschein DR, Karukstis KK, Scott MJ, Fuhrhop RJ, Scherer DE, Wickline SA. Targeted antiproliferative drug delivery to vascular smooth muscle cells with an MRI nanoparticle contrast agent: implications for rational therapy of restenosis. Circulation 2002;106:2842–2847.
8. Winter PM, Caruthers SD, Kassner A, Harris TD, Chinen LK, Allen JS, Zhang H, Robertson DJ, Wickline SA, Lanza GM. Molecular imaging of angiogenesis in nascent Vx-2 rabbit tumors using a novel avb3-targeted nanoparticle and 1.5 Tesla MRI. Cancer Res 2003;63:5838–5858.
9. Winter PM, Morawski AM, Caruthers SD, Fuhrhop RW, Zhang H, Williams TA, Allen JS, Robertson JD, Lanza GM, Wickline SA. Molecular imaging of angiogenesis in early-stage atherosclerosis with avb3-integrin-targeted nanoparticles. Circulation 2003;108:2270–2274.
10. Flacke S, Fischer S, Scott MJ, Fuhrhop RJ, Allen JS, Mclean M, Winter P, Sicard GA, Gaffney PJ, Wickline SA, Lanza GM. Novel MRI contrast agent for molecular imaging of fibrin: implications for detecting vulnerable plaques. Circulation 2001;104:1280–1285.
11. Yu X, Song S-K, Chen J, Scott MJ, Fuhrhop RJ, Hall CS, Gaffney PJ, Wickline SA, Lanza GM. High-resolution MRI characterization of human thrombus using a novel fibrin-targeted paramagnetic nanoparticle contrast agent. Magn Reson Med 2000;44:867–872.
12. Winter PM, Caruthers SD, Yu X, Song S-K, Fuhrhop RW, Scott MJ, Chen J, Miller B, Bulte JWM, Gaffney PJ, Wickline SA, Lanza GM. Improved molecular imaging contrast agent for early detection of unstable atherosclerotic plaques. Magn Reson Med 2003;50:411–416.
13. Landsberger S. Delayed instrumental neutron activation analysis. In: Alfassi ZB, editor. Chemical analysis by nuclear methods. New York: John Wiley & Sons; 1994. p 122–140.
14. Oltrona L, Speidel CM, Recchia D, Wickline SA, Eisenberg PR, Abendschein DR. Prolonged inhibition of tissue factor-mediated coagulation markedly attenuates stenosis after balloon-induced arterial injury in minipigs. Circulation 1997;96:646–652.
15. St. Pierre J, Yang L-Y, Tamirisa K, Scherrer D, Deciechi P, Eisenberg P, Tolunay E, Abendschein D. Tissue factor pathway inhibitor attenuates procoagulant activity and upregulation of tissue factor at the site of balloon-induced arterial injury in pigs. Arterioscler Thromb Vasc Biol 1999;19:2263–2268.
16. In den Kleef JJ, Cuppen JJ. RLSQ: T_1, T_2, and rho calculations, combining ratios and least squares. Magn Reson Med 1987;5:513–524.
17. Kirsch JE. Basic principles of magnetic resonance contrast agents. Top Magn Reson Imaging 1991;3:1–18.
18. Ahrens ET, Rothbacher U, Jacobs RE, Fraser SE. A model for MRI contrast enhancement using T_1 agents. Proc Natl Acad Sci USA 1998; 5:8443–8448.
19. Rose A. The sensitivity performance of the human eye on an absolute scale. J Opt Soc Am 1948;38:196–208.
20. Button TM, Fiel RJ. Isointense model for the evaluation of tumor-specific MRI contrast agents. Magn Reson Imaging 1988;6:275–280.
21. Unger EC, Totty WG, Neufeld DM, Otsuka FL, Murphy WA, Welch MS, Connett JM, Philpott GW. Magnetic resonance imaging using gadolinium labeled monoclonal antibody. Invest Radiol 1985;20:693–700.
22. Shreve P, Aisen AM. Monoclonal antibodies labeled with polymeric paramagnetic ion chelates. Magn Reson Med 1986;3:336–340.
23. Gillies RJ. In vivo molecular imaging. J Cell Biochem 2002;39(Suppl): 231–238.
24. Bulte JW, Douglas T, Witwer B, Zhang SC, Strable E, Lewis BK, Zywicke H, Miller B, van Gelderen P, Moskowitz BM, Duncan ID, Frank JA. Magneto-dendrimers allow endosomal magnetic labeling and in vivo tracking of stem cells. Nat Biotechnol 2001;19:1141–1147.
25. Hendrick RE, Haacke EM. Basic physics of MR contrast agents and maximization of image contrast. J Magn Reson Imaging 1993;3:137–148.
26. Ahrens ET, Rothbacher U, Jacobs RE, Fraser SE. A model for MRI contrast enhancement using T_1 agents. Proc Natl Acad Sci USA 1998; 95:8443–8448.
27. Hendrick RE, Nelson TR, Hendee WR. Optimizing tissue contrast in magnetic resonance imaging. Magn Reson Imaging 1984;2:193–204.
28. Nelson TR, Hendrick RE, Hendee WR. Selection of pulse sequences producing maximum tissue contrast in magnetic resonance imaging. Magn Reson Imaging 1984;2:285–294.
29. Perman WH, Hilal SK, Simon HE, Maudsley AA. Contrast manipulation in NMR imaging. Magn Reson Imaging 1984;2:23–32.
30. Look DC, Locker DR. Time saving in measurement of NMR and EPR relaxation times. Rev Sci Instrum 1970;41:250–251.
31. Allport JR, Weissleder R. In vivo imaging of gene and cell therapies. Exp Hematol 2001;29:1237–1246.
32. Wickline SA, Lanza GM. Nanotechnology for molecular imaging and targeted therapy. Circulation 2003;107:1092–1095.